left-sided heart can be obtained by projecting it to the LAP-CO plane. The preferential decrease in the pumping ability of the left-sided heart, such as seen in the ischemic heart disease, would rotate the projected curve to the RAP-LAP plane to the direction of LAP axis.

Third, the blood-pooling ability of the vasculature and the effect of stressed blood on the vasculature can be expressed by the venous return surface (Fig. 1, shaded surface). This surface remains the same so long as the total stressed volume is unchanged irrespective of its distribution. Increased LAP and pulmonary congestion associated with left-sided heart failure is characterized by blood redistribution from systemic to pulmonary vascular beds. Blood redistribution, however, would not change the venous return surface itself (i.e., unaffected by the changes in pumping ability). This is in sharp contrast with the classical venous return curve of Guyton's model. The relatively flat slope of the surface to the direction of LAP axis indicates the smaller blood-pooling ability of pulmonary vascular beds. As a result, the decrease in RAP with systemic-to-pulmonary blood redistribution is much smaller than the increase in LAP. This is shown, also illustratively in Fig. 1, by moving along the venous return surface and parallel to the RAP-LAP plane (keeping CO constant).

B. Animal Experiments to Characterize Cardiac Output Curve

We planned to characterize both cardiac output curve and venous return surface as precisely as possible in animals by using even the most invasive methods. In characterizing the pumping ability, only the heart of animals is needed; in characterizing the blood-pooling ability, only the vasculature of animals is needed.

The experiment for the characterization of cardiac output curve was less invasive. We do not need to physically detach the vasculature from the heart. Rather, in 7 dogs, by withdrawing and transfusing blood in a stepwise manner, we were able to obtain both right- and left-sided cardiac output curve simultaneously.

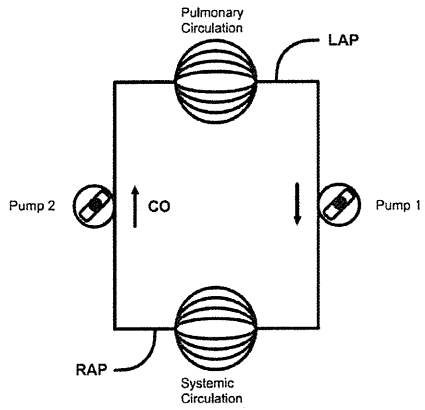

Fig. 2. An experimental scheme to characterize venous return surface. By replacing the right- and the left-sided heart with respective roller pumps, one can change cardiac output of the right- and the left-sided heart independently.

C. Animal Experiments to Characterize Venous Return Surface

Figure 2 depicts the scheme of an experiment to characterize the venous return surface. To extract only the vasculature and to physically remove the animal heart from the cardiovascular system, we replaced the right- and the left-sided heart with respective roller pumps. These pumps allow us to change CO of the right- and left-sided heart independently. Changing the flow of the two pumps at the same level would simulate the weak or strong heart. Transient unbalancing flow would redistribute blood between systemic and pulmonary vascular beds.

In each of 6 canine preparations, we obtained 6 different hemodynamic (CO, RAP, LAP) data sets. In each animal, these sets of data were fit to a flat surface in 3D coordinate system by linear regression analysis. CO was selected as a dependent variable and RAP (~2-5 mmHg) and LAP (~0-10 mmHg) are selected as independent variables.

D. Method to Estimate Cardiac Output Curve from a Single Hemodynamic Data Set

We fit experimental data to two logarithmic curves (one for the right- and the other for the left-sided heart), based on the knowledge of exponential end-diastolic pressure volume relationship and linear end-systolic pressure volume relationship, as follows.

$$CO = S\,[\ln(P - A) + B]$$

Here, P indicates RAP or LAP; A, B, and S are parameters. As analytical solution indicated that A and B is only dependent on diastolic properties of the ventricles, and is unlikely to change acutely, we fixed these parameters as their respective average values. This enabled one to estimate cardiac output curve from a single hemodynamic data set.

E. Method to Estimate Venous Return Surface from a Single Hemodynamic Data Set

We were able to fit experimental data to a flat surface well (r^2=0.92 to 0.99). As the surfaces from 6 animals were reasonably parallel (see Results), we used average slopes to estimate venous return surface from a single hemodynamic data set. Furthermore, as CO-axis intercept was linearly related to the withdrawn or transfused blood volume, we used this relationship to estimate a new venous return surface after blood volume change.

III. Results

A. Method to Estimate Cardiac Output Curve from a Single Hemodynamic Data Set

We were able to fit the cardiac output curve of both the right- and the left-sided heart by logarithmic functions (right-sided heart, r^2=0.90 to 0.99; left-sided heart, r^2=0.95 to 0.99). Since standard deviation of parameter A (1.29) or that of parameter

B (1.25) was much smaller than that of parameter S (30.9), we used the respective average values for A and B. The obtained cardiac output curves for right- and left-sided heart were as follows.

$$CO = S_R [\ln(RAP - 2.13) + 1.90] \quad (1)$$

$$CO = S_L [\ln(LAP - 2.03) + 0.80] \quad (2)$$

Parameters S_R and S_L can be used to represent the magnitude of the pumping ability of the right- and left-sided heart, respectively. As S_R and S_L can be calculated from a single set of hemodynamic data, we can approximately get cardiac output curve.

B. Method to Estimate Cardiac Output Curve from a Single Hemodynamic Data Set

In Figure 3 we have shown the venous return surfaces obtained from all 6 dogs. The surfaces were shown (as if they were lines) from the direction parallel to the surface. The figure indicates that in each of 6 dogs, all 6 data sets are located very near the flat surface. This implied the goodness of the fit of these data points to the flat surface. It is also shown that three coordinate axes are almost parallel among these dogs. This is because the slopes of the surface were almost the same among animals. These experimental results indicated that the venous return surface is linear and can be expressed by a common equation for all animals.

$$CO = CO_{max} - 19.61\ RAP - 3.49\ LAP.$$

Further, by infusing or withdrawing known amounts of blood, we were able to relate CO_{max} to blood volume as

$$CO_{max} = V / 0.129 \quad (3)$$

where V is total intravascular stressed blood volume. Combining these equations resulted in

$$CO = V / 0.129 - 19.61\ RAP - 3.49\ LAP. \quad (4)$$

Parameter V can be used to monitor the changes in total stressed blood volume. As V can be calculated from a single set of hemodynamic data, we can approximately get venous return surface.

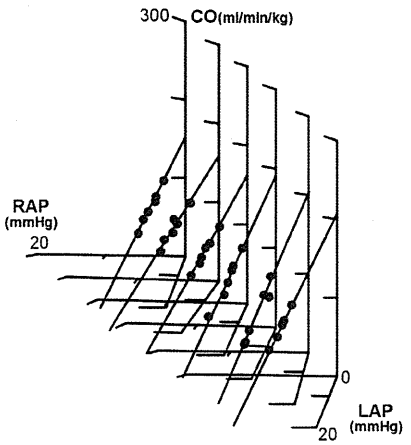

Fig. 3. Venous return surfaces obtained from 6 dogs. For each dog, the venous return surface was projected in a direction parallel to the surface, and was superimposed with each other.

C. Prediction of New Hemodynamics after Volume Change

We predicted new hemodynamics after volume change as follows. First, baseline cardiac output curve (Equations 1 and 2) and venous return surface (Equation 4) were approximately estimated from a single baseline hemodynamic data, by the methods shown in two previous sections IIIA and IIIB. Next, a new venous return surface was estimated by changing CO_{max} according to Equation 3. We assumed that cardiac output curve would not change by the volume change. Finally, new hemodynamics data were estimated by calculating the intersection between cardiac output curve and venous return surface.

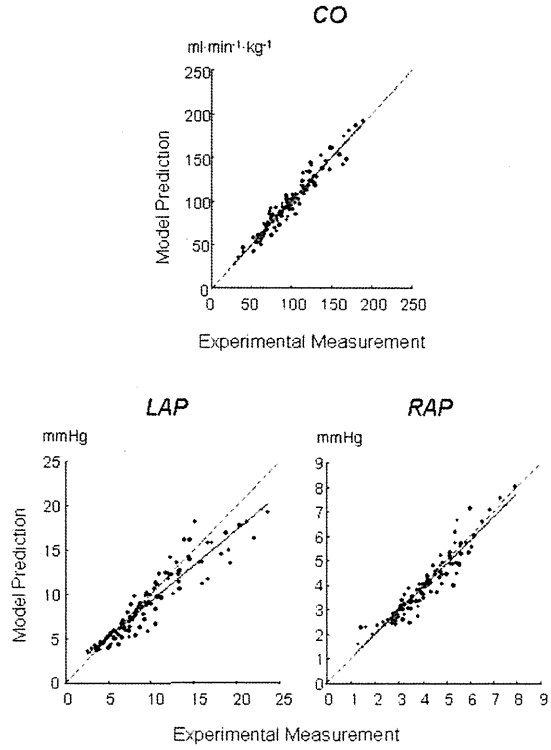

Fig. 4. Prediction of CO, LAP, and RAP from estimated cardiac output curve and venous return surface after volume change.

Using these new estimated cardiac output curve and venous return surface, we were able to predict the hemodynamics (y value) after withdrawal or transfusion of blood of known volume precisely as compared to actually measured (x value) (CO: $y = 0.93x + 6.5$, $r^2 = 0.96$, SEE [standard error of estimate] = 7.5 $ml \cdot min^{-1} \cdot kg^{-1}$; LAP: $y = 0.90x + 0.5$, $r^2 = 0.93$, SEE = 1.4 mmHg; RAP: $y = 0.87x + 0.4$, $r^2 = 0.91$, SEE = 0.4 mmHg) (Fig. 4) [3].

IV. Discussion

A. Most Undiagnosed Property: Total Stressed Blood Volume

The three major players of the cardiovascular system are heart

(pumps), vasculature (tubes with resistive and capacitive function), and blood. These three components interactively determine all hemodynamic variables. Of these, pump function and resistive function of vasculature have been repeatedly evaluated in previous studies. These properties were also evaluated clinically.

In contrast, evaluation of the vascular capacitive function and that of the blood volume have been relatively ignored. Even though blood volume drastically changes, there have been no reasonable methods to evaluate total stressed blood volume precisely. Simple measurement of central venous pressure (i.e., RAP) cannot be a proxy marker of blood volume, as this pressure value also changes with pump function or with redistribution of blood.

It is clear from our results [$V = (CO + 19.61\ RAP + 3.49\ LAP) \times 0.129$] that blood volume (V) is not solely determined by RAP. Rather, all three variables CO, RAP and LAP contribute (not as differently as have been considered) to the changes in blood volume. Clinicians should know that when LAP increases by 5.6 mmHg, or CO increases by 0.98L/min in 50-Kg patients, similar blood volume increases as RAP is increased by 1 mmHg.

Implantable devices with volume monitoring functionality for patients with heart failure should also take these results into consideration.

B. Hemodynamic Variables and Cardiovascular Properties

In clinical practice, physicians have to restore hemodynamic variables to their respective normal range. Of these, the most important three variables include blood pressure, CO and LAP. These variables are essentially important as blood pressure determines the perfusion of vital organs (for short-term need), CO determines the perfusion of peripheral tissues (for long-term need), and LAP determines blood oxygenation in lungs.

These hemodynamic variables are, in turn, determined by the interaction between cardiovascular properties, such as pump, resistance, capacitance, and blood volume. What clinicians should know, monitor, and correct are in reality these cardiovascular properties. Most drugs and interventions are aimed at correcting mainly one of these properties. From these viewpoints, the method to continuously estimate cardiovascular properties from measured hemodynamics is the most basic need in patient monitoring.

V. CONCLUSION

We have successfully developed a method to estimate the cardiac output curve and venous return surface from a single hemodynamic data set. This method enabled to predict new hemodynamics after withdrawal or transfusion of blood of known volume.

REFERENCES

[1] A. C. Guyton, "Determination of cardiac output by equating venous return curves with cardiac response curves," *Physiol. Rev.* vol. 35, no. 1,123–129, Jan. 1955.

[2] K. Uemura, M. Sugimachi, T. Kawada, A. Kamiya, Y. Jin, *et al.*, "A novel framework of circulatory equilibrium," *Am. J. Physiol. Heart Circ. Physiol.* vol. 286, no. 6, pp. H2376–H2385, Jun. 2004.

[3] K. Uemura, T. Kawada, A. Kamiya, T. Aiba, I. Hidaka, *et al.*, "Prediction of circulatory equilibrium in response to changes in stressed blood volume," *Am. J. Physiol. Heart Circ. Physiol.* vol. 289, no. 1, H301–H307, Jul. 2005.

J Physiol Sci (2010) 60:407–413
DOI 10.1007/s12576-010-0109-8

ORIGINAL PAPER

Both skeletonized and pedicled internal thoracic arteries supply adequate graft flow after coronary artery bypass grafting even during intense sympathoexcitation

Dai Une · Shuji Shimizu · Atsunori Kamiya · Toru Kawada · Toshiaki Shishido · Masaru Sugimachi

Received: 21 February 2010 / Accepted: 15 August 2010 / Published online: 14 September 2010

Abstract The internal thoracic artery (ITA) is harvested by either the pedicled or the skeletonized technique in coronary artery bypass grafting (CABG), with no clear advantage of one technique over the other. We compared graft flow between the pedicled and skeletonized ITA grafts while varying myocardial oxygen demand. CABG was performed to the left anterior descending artery in five anesthetized dogs using a pedicled ITA graft and the graft was subsequently skeletonized. Graft flow was measured during stepwise electrical stimulation of the stellate ganglion. The baseline graft flow before sympathetic stimulation was higher in skeletonized (27.8 ± 1.9 ml/min) than that in pedicled ITA grafts (22.6 ± 2.7 ml/min) ($P < 0.05$). In both ITA grafts, however, graft flow increased to a similar level during sympathetic stimulation that doubled the double product, correlating with the double product. Based on these results, we conclude that metabolic demand can override the potential difference in sympathetic vasoconstriction in both pedicled and skeletonized ITA grafts.

Keywords Coronary artery bypass grafting · Graft flow · Internal thoracic artery · Pedicled · Skeletonized · Sympathetic activation

D. Une · S. Shimizu (✉) · A. Kamiya · T. Kawada · T. Shishido · M. Sugimachi
Department of Cardiovascular Dynamics, National Cerebral and Cardiovascular Center Research Institute, 5-7-1 Fujishiro-dai, Suita, Osaka 565-8565, Japan
e-mail: shujismz@ri.ncvc.go.jp

S. Shimizu
Japan Association for the Advancement of Medical Equipment, Tokyo, Japan

Introduction

The internal thoracic artery (ITA) is the gold standard conduit for coronary artery bypass grafting (CABG) because of its long-term patency [1]. The ITA is harvested by either the pedicled or the skeletonized technique, and which of these two techniques is the better option has been the subject of an extended debate—with as yet no clear conclusion being drawn. Although some human studies [2–4] have demonstrated higher free (pre-anastomosis) flow through skeletonized grafts (with or without topical papaverine), suggesting that the loss of sympathetic nerve-mediated graft vasoconstriction confers an advantage, perfusion pressure was not controlled in these studies. In one study [5] in which the perfusion pressure was controlled, free flow even tended to be lower in skeletonized grafts prior to the administration of intravenous papaverine. Onorati et al. [6] found that graft flows were comparable between the two techniques in the absence of intraluminal papaverine, while Takami and Ina [7], in a comparison of the flow through the anastomosed graft, found that flow was higher through the skeletonized graft.

Flow in the anastomosed graft is likely to be largely dependent on myocardial oxygen demand, suggesting the importance of comparing the flow between the pedicled and skeletonized ITA grafts under varying conditions of myocardial oxygen demand. If the skeletonization procedure were to result in an increased flow capacity, surgeons may be able to perform additional anastomoses to other vessels using the skeletonized ITA, thereby making the skeletonized ITA procedure even more advantageous. If the skeletonization procedure were not able to increase flow capacity, the skeletonized ITA would not be recommended for additional use due to a higher flow reserve. We hypothesized that the skeletonized ITA would have larger

flow capacity due to the loss of sympathetic nerve-mediated graft vasoconstriction.

Materials and methods

Animal preparation

Animal care was provided in accordance with the *Guiding Principles for the Care and Use of Animals in the Field of Physiological Sciences* approved by the Physiological Society of Japan. All protocols were approved by the Animal Subject Committee of the National Cerebral and Cardiovascular Center. Five adult mongrel dogs (weighing 24–35 kg) were anesthetized with intravenous pentobarbital sodium (25 mg/kg) and intubated endotracheally for artificial ventilation with isoflurane and 100% O_2. After a median sternotomy, the heart was suspended in a pericardial cradle. To measure systemic arterial pressure, we placed a fluid-filled catheter in the left subclavian artery via the left brachial artery and connected it to a pressure transducer (DX-200; Nihon Kohden, Tokyo, Japan). The junction of the inferior vena cava and the right atrium was taken as the reference point for zero pressure. An ultrasonic flowmeter (20A594; Transonic Systems, Itaca, NY) was placed around the ascending aorta to measure cardiac output. Electrocardiography leads were also placed for the monitoring electrocardiogram. A catheter was inserted into the femoral vein for fluid replacement (1 ml/kg/h of Ringer's solution). All protocols were performed under open chest conditions.

Pedicled ITA grafting

The left internal thoracic artery (LITA), together with the surrounding veins, muscle, and fascia, was harvested as a pedicled graft using electrocautery. The LITA was harvested from the bifurcation of the musculo-phrenic and superior epigastric arteries up to the upper margin of the first rib or higher. All intercostal branches of the LITA were ligated. After systemic heparinization, the LITA was clamped, and the distal end of the LITA was cut and anastomosed to the left anterior descending artery (LAD). The same surgeon (D.U.) performed the LITA–LAD anastomosis without cardiopulmonary bypass. The heart and the LAD were stabilized using a compression-type mechanical stabilizer (Mini-CABG system; United States Surgical Corporation, Norwalk, CT). A shunt tube was inserted into the LAD to prevent myocardial ischemia during anastomosis. The anastomosis was placed in the mid-LAD [8]. The anastomosis was created using a continuous 7-0 polypropylene suture. The proximal LAD was first ligated after the LITA–LAD anastomosis, and then the LITA was declamped. An angiography was performed after the anastomosis to confirm the absence of stenosis or spasm in the LITA–LAD anastomosis. The LITA graft was sprayed with dilute papaverine (4 mg/ml) to prevent spasm. An ultrasonic flowmeter (2.5S261; Transonic Systems) was placed around the LITA just proximal to the anastomosis. The left stellate ganglion was carefully exposed through a median sternotomy, and a pair of platinum electrodes was attached to it without decentralization. The nerve and electrodes were covered with a mixture of silicone gel (Kwik-Sil; World Precision Instrument, Sarasota, FL). Protocol 1, described below, was carried out following the pedicled LITA grafting.

Skeletonized ITA grafting

Following the completion of protocol 1, the tissue surrounding the graft (including fascia and lymphatics) was stripped up to the most proximal part of the LITA graft in order to skeletonize the LITA graft. The side branches of the LITA were ligated. Fat tissue around the graft was removed as completely as possible based on macroscopic inspection. The adventitia was left as the outermost layer of the graft. The graft was not touched directly with forceps. The graft was sprayed with dilute papaverine (4 mg/ml). After skeletonizing the LITA graft, protocol 2 followed.

Experimental protocols

Since skeletonization always followed pedicled harvesting, protocol 1 (pedicled LITA graft flow measurement) was performed before protocol 2 (skeletonized LITA graft flow measurement) in all dogs. The stimulation of the left sympathetic stellate ganglion for adjusting the voltage amplitude was performed at least 30 min before protocol 1 was initiated.

Protocol 1

The left sympathetic stellate ganglion was electrically stimulated at least 30 min after the completion of the experimental preparation of the pedicled LITA grafts. The frequency of stimulation was increased stepwise from 0 to 10 Hz with increments of 2 Hz. Each step was maintained for 60 s. The pulse duration of the stimulus was set at 5 ms. The voltage amplitude of stimulation (2–5 V) was adjusted in each animal to yield an increase in arterial pressure of approximately 30 mmHg with 10 Hz stimulation. Graft flow, arterial pressure, and cardiac output were recorded for 7 min, which included a 2-min baseline and 5 min of stimulation. These data were sampled at 200 Hz using a 12-bit analog-to-digital converter [AD12-16U(PCI)E;

CONTEC, Osaka, Japan] and stored on the hard disk of a dedicated laboratory computer system.

Protocol 2

At least 30 min after the completion of the experimental preparation of the skeletonized LITA grafts, the left sympathetic stellate ganglion was electrically stimulated in a similar fashion to protocol 1, while all variables were recorded and stored.

Data analysis

Heart rate was calculated from the arterial pressure waveform. Myocardial oxygen demand was estimated as double product (pressure–rate product) and calculated as the product of systolic arterial pressure and heart rate [9]. All variables were averaged during the last 20 s of each electrical stimulation level.

Statistical analysis

All data are presented as the mean ± standard error (SE). In each protocol, one-way repeated measures analysis of variance (ANOVA) followed by Dunnett's test was used to compare variables at each stimulation against the baseline value. The paired t test was used to compare variables between pedicled and skeletonized LITA grafts at each stimulation level. Linear regression analysis was used to examine the relationship between the double product and graft flow. Differences were considered to be significant at a threshold of $P < 0.05$.

Results

Prior to sympathetic stimulation, baseline graft flow (under spontaneous sympathetic outflow) was greater in skeletonized ITA than pedicled ITA (Table 1). Other hemodynamic parameters, including heart rate, cardiac output, mean arterial pressure, and double product, did not differ significantly regardless of harvesting technique.

Table 1 Hemodynamic parameters and graft flow before stimulation

Hemodynamic parameters	Pedicled	Skeletonized	P value
Heart rate (beats/min)	104 ± 8	106 ± 8	NS
Mean arterial pressure (mmHg)	94 ± 7	93 ± 7	NS
Cardiac output (ml/min/kg)	83 ± 17	74 ± 9	NS
Double product (mmHg beats/min)	11368 ± 834	11346 ± 621	NS
Graft flow before stimulation (ml/min)	22.6 ± 2.7	27.8 ± 1.9	<0.05

Values are given as the mean ± standard error (SE)

NS Not significant

Graft flow patterns at baseline and under sympathetic stimulation are shown in Fig. 1a. Sympathetic stimulation increased graft flow ($P < 0.05$) similarly in skeletonized and pedicled ITA grafts, and maximal flow was comparable to each other at 10-Hz stimulation [nonsignificant (NS) difference] (Fig. 1b). Increases in systemic arterial pressure and heart rate did not differ significantly between the two techniques (Fig. 2), and increases in myocardial oxygen demand in response to sympathetic stimulation, as estimated by double product, were likewise similar.

Graft flow (y) correlated well with the double product (x) in both pedicled ($y = 2.6 \times 10^{-3}x - 8.4$, $R^2 = 0.73$) and skeletonized ITA ($y = 2.3 \times 10^{-3}x - 0.7$, $R^2 = 0.69$). The slope and y-intercept did not differ statistically between the two techniques (Fig. 3).

Discussion

The choice of either skeletonized or pedicled ITA grafts for CABG may be an important decision from both the technical and clinical viewpoints; however, clear evidence demonstrating the advantage of either method over the other is not yet available. In this study, we have shown that graft flow increased to a similar level during maximal sympathetic stimulation in both pedicled and skeletonized ITA grafts. These results do not support our hypothesis that the skeletonized ITA would provide larger flow capacity and indicate that coronary vasodilatation in response to increased myocardial oxygen demand is a stronger determinant of graft flow than any possible increase in the vascular resistance of ITA itself. Our study also demonstrates that both skeletonized and pedicled ITAs were able to supply adequate graft flow after CABG even during intense sympathoexcitation.

There are several possible explanations for the difference in graft flow under baseline conditions. First, a loss of sympathetic innervation in the skeletonized graft may have dilated the ITA relative to the pedicled graft under baseline conditions. In support of this explanation, Takami et al. [7] reported that the diameter of the ITA just proximal to the anastomosis is significantly larger in the skeletonized ITA than that in the pedicled ITA. Dönmez et al. [10] reported that the diameter of ITA becomes statically larger by the stellate ganglion blockade. In a preliminary study, we observed that electrical stimulation of the stellate ganglion decreased ITA flow before harvest. Therefore, vasoconstriction may occur in the pedicled ITA during sympathetic stimulation. However, in this study we did not perform simultaneous measurements of the graft flow and diameter

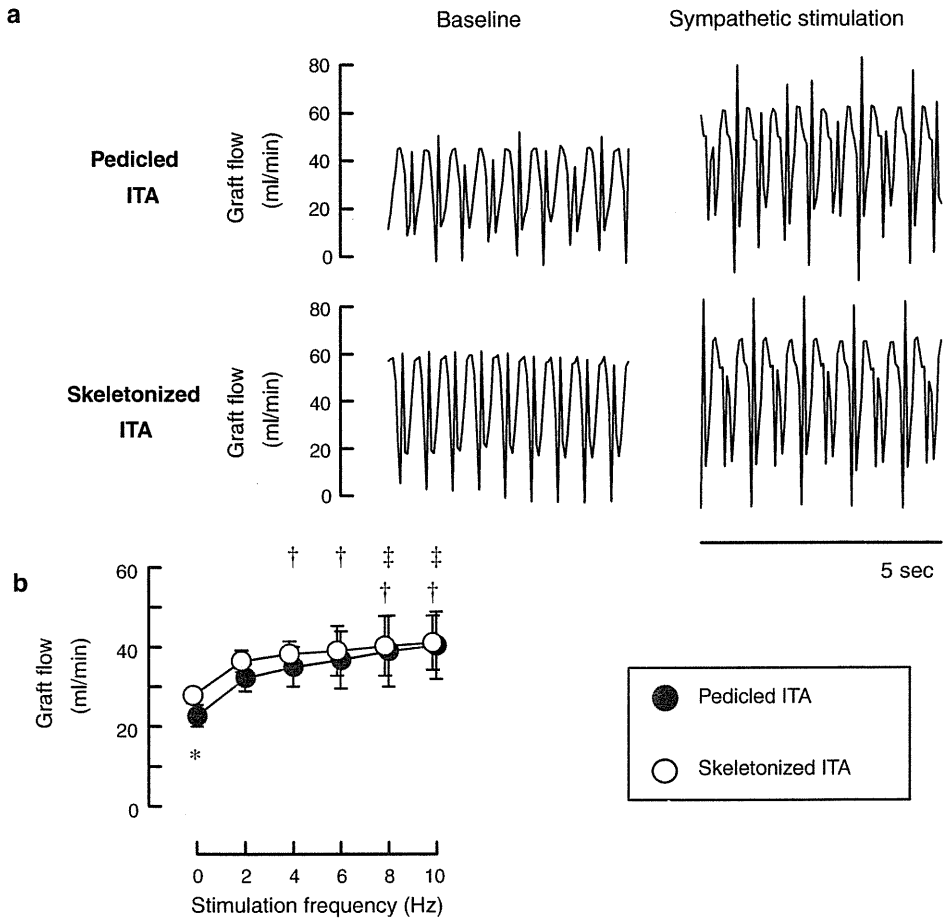

Fig. 1 **a** Typical representative recording of graft flow with pedicled and skeletonized internal thoracic arteries (*ITAs*) during sympathetic nerve stimulation. **b** Mean graft flow with pedicled (*closed circle*) and skeletonized (*open circle*) ITAs during sympathetic nerve stimulation. Data are shown as the mean ± standard error (SE). $^{\dagger}P < 0.05$ vs. baseline, $^{\ddagger}P < 0.01$ vs. baseline, $^{*}P < 0.05$ pedicled vs. skeletonized

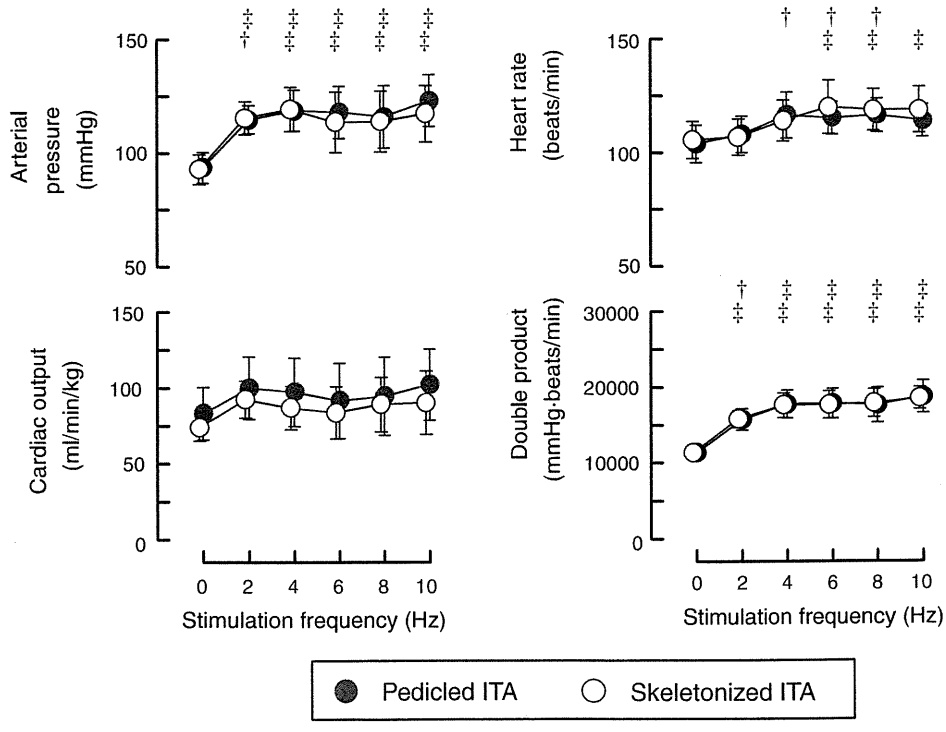

Fig. 2 Changes in mean arterial pressure, cardiac output, heart rate, and double product with pedicled (*closed circle*) and skeletonized (*open circle*) ITAs during sympathetic nerve stimulation. Data are shown as the mean ± SE. $^{\dagger}P < 0.05$ vs. baseline, $^{\ddagger}P < 0.01$ vs. baseline

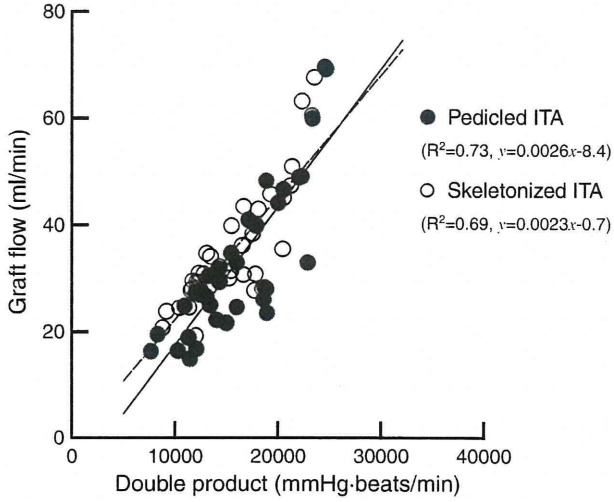

Fig. 3 Scatter plots and regressions between the double product and graft flow with pedicled (*closed circle, solid line*) and skeletonized (*open circle, dashed line*) ITAs. Regression lines did not differ between the two groups. y Graft flow, x double product

because the use of contrast medium in angiography may have affected the graft flow through its vasodilatative effect on the coronary artery [11].

Another explanation may be the difference in background sympathetic tone. As the skeletonized graft flow was always studied in the later phase of the experiment, when background sympathetic tone and myocardial metabolic demand may be higher, skeletonized graft flow may have been higher for this reason. The presence of similar hemodynamics during the two protocols, however, does not directly support this explanation. The hemodilution seen predominantly in the later phase of the experiment may also have contributed to higher flow through the skeletonized graft under baseline conditions.

The fact that graft flows were similar between the skeletonized and pedicled ITAs during maximal sympathetic excitation indicates that the resistance of the ITA graft was much smaller than that of the native coronary bed, even when the coronary bed was maximally dilated to meet the oxygen demand present with maximal sympathetic stimulation. In other words, both the skeletonized and pedicled ITAs would appear to provide sufficient flow reserve to the LAD area. In contrast, it has been reported that free flow, which may represent the maximal flow capacity of the ITA itself, is greater in the skeletonized ITA than in the pedicled ITA [2, 3]. Despite these previous findings, because the maximally dilated native coronary bed would be the most practical downstream conduit to test the difference between the skeletonized and pedicled ITAs, we believe that the difference in sympathetic innervation does not affect the maximal flow significantly under anastomosed conditions.

In addition to the effects of downstream resistance, local mechanisms would also contribute to the observed difference in flow between the pedicled and skeletonized ITA grafts. Complete sympathetic denervation with the local application of phenol to the skeletonized ITA further increased graft flow (unpublished observation), suggesting that there remains a certain sympathetic innervation in the skeletonized ITA. Even though sympathetic denervation may not be complete after skeletonization, we believe that our skeletonization did not differ greatly from those clinically performed by surgeons. Deja et al. [4] reported that skeletonization increases the reactivity of ITA to norepinephrine in vitro. Their study may support our results. Prior to sympathetic stimulation but under spontaneous sympathetic outflow, the amount of endogenous norepinephrine release to the skeletonized ITA may be relatively smaller than that to the pedicled ITA; as such, the sympathetic vasoconstriction would be negligible in the skeletonized ITA. This may explain the larger graft flow in the skeletonized ITA prior to sympathetic stimulation. Under maximal sympathetic stimulation, however, hyperreactivity to endogenous norepinephrine in the skeletonized ITA may cause the sympathetic vasoconstriction similar to that occurring in the pedicled ITA. This local mechanism may also partly account for why graft flow was comparable between the pedicled and skeletonized ITAs during maximal sympathetic stimulation. Although the results from several pharmacological studies suggest that norepinephrine-induced vasoconstriction does occur in the ITA [12, 13], there have been no reports assessing the tissue norepinephrine concentration of ITA during sympathetic stimulation. Further investigations are necessary to gain an understanding of the difference in norepinephrine reactivity between the pedicled and skeletonized ITAs.

Some publications have reported several advantages of the skeletonized ITA grafts other than the potential increase in graft flow at rest [1, 14]. Firstly, skeletonization lengthens the ITA, thereby providing access to more distal targets in the coronary artery [15]. Second, skeletonization improves blood supply to the sternum (measured by single photon emission computed tomography) [16] compared with pedicled harvesting. Third, skeletonization decreases the incidence of postoperative respiratory dysfunction because of less invasive harvesting (i.e., preserved pleural integrity in skeletonized ITA vs. pleurotomy in pedicled ITA) [17, 18]. Lastly, skeletonization markedly reduces anterior chest pain and dysesthesia 3 months after surgery [19]. In contrast to these advantages, skeletonization has the minor disadvantages of greater technical difficulty, longer harvesting duration, and potential damage to the graft.

Limitations

This study has several limitations. First, because skeletonized graft flow measurements always follow pedicled graft flow measurements in the same dog, the effect of time sequence on graft flows cannot be ruled out. Nevertheless, the similar hemodynamic response to sympathetic stimulation between protocol 1 and 2 (Fig. 2) suggests that the animal conditions did not deteriorate considerably. Second, the perfusion area of LITA was limited to the LAD region. If we had used a much larger perfusion area of LITA, the possible small difference between the pedicled and skeletonized ITAs may have been revealed. Third, a histological comparison between the pedicled and skeletonized ITA was not performed because the pedicled ITA was always skeletonized after the protocol 1, and the tissue samples from the pedicled ITA could not be obtained. Further investigations that include histological comparison are necessary for examining the effect of skeletonization on sympathetic innervations.

Conclusion

Both the pedicled and skeletonized ITA techniques supplied similar, adequate blood flow to the LAD, meeting myocardial oxygen demand during sympathetic excitation. Metabolic demand can override the possible difference in sympathetic vasoconstriction, increasing the flow in both pedicled and skeletonized ITA grafts to a similar extent when they are anastomosed to LAD. The results of this study have an important implication in terms of clinical application. Following anastomosis, graft flow is highly variable and is dependent on myocardial oxygen demand. Because the quality of CABG may be judged based on flow through anastomosed grafts, one has to take into consideration the potential change in flow in response to myocardial oxygen demand.

Acknowledgments This study was supported by Health and Labor Sciences Research Grants (H18-nano-Ippan-003, H19-nano-Ippan-009, H20-katsudo-Shitei-007 and H21-nano-Ippan-005) from the Ministry of Health, Labor and Welfare of Japan, by Grants-in-Aid for Scientific Research (No. 20390462) from the Ministry of Education, Culture, Sports, Science and Technology in Japan and by the Industrial Technology Research Grant Program from New Energy and Industrial Technology Development Organization (NEDO) of Japan.

References

1. Del Campo C (2003) Pedicled or skeletonized? A review of the internal thoracic artery graft. Tex Heart Inst J 30:170–175
2. Castro GP, Dussin LH, Wender OB, Barbosa GV, Saadi EK (2005) Comparative analysis of the flows of left internal thoracic artery grafts dissected in the pedicled versus skeletonized manner for myocardial revascularization surgery. Arq Bras Cardiol 84:261–266
3. Deja MA, Woś S, Gołba KS, Zurek P, Domaradzki W, Bachowski R, Spyt TJ (1999) Intraoperative and laboratory evaluation of skeletonized versus pedicled internal thoracic artery. Ann Thorac Surg 68:2164–2168
4. Deja MA, Gołba KS, Malinowski M, Woś S, Kolowca M, Biernat J, Kajor M, Spyt TJ (2005) Skeletonization of internal thoracic artery affects its innervation and reactivity. Eur J Cardiothorac Surg 28:551–557
5. Wendler O, Tscholl D, Huang Q, Schäfers HJ (1999) Free flow capacity of skeletonized versus pedicled internal thoracic artery grafts in coronary artery bypass grafts. Eur J Cardiothorac Surg 15:247–250
6. Onorati F, Esposito A, Pezzo F, di Virgilio A, Mastroroberto P, Renzulli A (2007) Hospital outcome analysis after different techniques of left internal mammary grafts harvesting. Ann Thorac Surg 84:1912–1919
7. Takami Y, Ina H (2002) Effects of skeletonization on intraoperative flow and anastomosis diameter of internal thoracic arteries in coronary artery bypass grafting. Ann Thorac Surg 73:1441–1445
8. Austen WG, Edwards JE, Frye RL, Gensini GG, Gott VL, Griffith LS, McGoon DC, Murphy ML, Roe BB (1975) A reporting system on patients evaluated for coronary artery disease. Report of the Ad Hoc Committee for Grading of Coronary Artery Disease, Council on Cardiovascular Surgery, American Heart Association. Circulation 51:5–40
9. Kitamura K, Jorgensen CR, Gobel FL, Taylor HL, Wang Y (1972) Hemodynamic correlates of myocardial oxygen consumption during upright exercise. J Appl Physiol 32:516–522
10. Dönmez A, Tufan H, Tutar N, Araz C, Sezgin A, Karadeli E, Torgay A (2005) In vivo and in vitro effects of stellate ganglion blockade on radial and internal mammary arteries. J Cardiothorac Vasc Anesth 19:729–733
11. Baile EM, Paré PD, D'yachkova Y, Carere RG (1999) Effect of contrast media on coronary vascular resistance: contrast-induced coronary vasodilation. Chest 116:1039–1045
12. Evora PR, Pearson PJ, Discigil B, Oeltjen MR, Schaff HV (2002) Pharmacological studies on internal mammary artery bypass grafts. Action of endogenous and exogenous vasodilators and vasoconstrictors. J Cardiovasc Surg (Torino) 43:761–771
13. He GW, Yang CQ, Starr A (1995) Overview of the nature of vasoconstriction in arterial grafts for coronary operations. Ann Thorac Surg 59:676–683
14. Athanasiou T, Crossman MC, Asimakopoulos G, Cherian A, Weerasinghe A, Glenville B, Casula R (2004) Should the internal thoracic artery be skeletonized? Ann Thorac Surg 77:2238–2246
15. Higami T, Yamashita T, Nohara H, Iwahashi K, Shida T, Ogawa K (2001) Early results of coronary grafting using ultrasonically skeletonized internal thoracic arteries. Ann Thorac Surg 71:1224–1228
16. Cohen AJ, Lockman J, Lorberboym M, Bder O, Cohen N, Medalion B, Schachner A (1999) Assessment of sternal vascularity with single photon emission computed tomography after harvesting of the internal thoracic artery. J Thorac Cardiovasc Surg 118:496–502
17. Bonacchi M, Prifti E, Giunti G, Salica A, Frati G, Sani G (2001) Respiratory dysfunction after coronary artery bypass grafting employing bilateral internal mammary arteries: the influence of intact pleura. Eur J Cardiothorac Surg 19:827–833
18. Matsumoto M, Konishi Y, Miwa S, Minakata K (1997) Effect of different methods of internal thoracic artery harvest on pulmonary function. Ann Thorac Surg 63:653–655

19. Boodhwani M, Lam BK, Nathan HJ, Mesana TG, Ruel M, Zeng W, Sellke FW, Rubens FD (2006) Skeletonized internal thoracic artery harvest reduces pain and dysesthesia and improves sternal perfusion after coronary artery bypass surgery: a randomized, double-blind, within-patient comparison. Circulation 114:766–773

J Physiol Sci (2010) 60:283–298
DOI 10.1007/s12576-010-0096-9

ORIGINAL PAPER

Open-loop dynamic and static characteristics of the carotid sinus baroreflex in rats with chronic heart failure after myocardial infarction

Toru Kawada · Meihua Li · Atsunori Kamiya · Shuji Shimizu · Kazunori Uemura · Hiromi Yamamoto · Masaru Sugimachi

Received: 24 January 2010 / Accepted: 5 May 2010 / Published online: 1 June 2010

Abstract We estimated open-loop dynamic characteristics of the carotid sinus baroreflex in normal control rats and chronic heart failure (CHF) rats after myocardial infarction. First, the neural arc transfer function from carotid sinus pressure to splanchnic sympathetic nerve activity (SNA) and its corresponding step response were examined. Although the steady-state response was attenuated in CHF, the negative peak response and the time to peak did not change significantly, suggesting preserved neural arc dynamic characteristics. Next, the peripheral arc transfer function from SNA to arterial pressure (AP) and its corresponding step response were examined. The steady-state response and the initial slope were reduced in CHF, suggesting impaired end-organ responses. In a simulation study based on the dynamic and static characteristics, the percent recovery of AP was reduced progressively as the size of disturbance increased in CHF, suggesting that a reserve for AP buffering is lost in CHF despite relatively maintained baseline AP.

T. Kawada (✉) · M. Li · A. Kamiya · S. Shimizu · K. Uemura · M. Sugimachi
Department of Cardiovascular Dynamics, National Cerebral and Cardiovascular Center Research Institute, 5-7-1 Fujishirodai, Suita, Osaka 565-8565, Japan
e-mail: torukawa@res.ncvc.go.jp

M. Li · S. Shimizu
Japan Association for the Advancement of Medical Equipment, Tokyo 113-0033, Japan

H. Yamamoto
Division of Cardiology, Department of Internal Medicine, Kinki University School of Medicine, Osaka 589-8511, Japan

Keywords Systems analysis · Transfer function · White noise · Sympathetic nerve activity · Arterial pressure · Equilibrium diagram

Introduction

The arterial baroreflex is an important negative feedback system that stabilizes systemic arterial pressure (AP) against exogenous disturbances. The rapidness of AP regulation may be best described by the system dynamic characteristics. With respect to the sympathetic arterial baroreflex system, previous studies in rabbits [1] and rats [2] have indicated that the transfer function of the baroreflex neural arc from baroreceptor pressure input to efferent sympathetic nerve activity (SNA) exhibits "derivative" characteristics, which means that the dynamic gain of the SNA response to pressure perturbation becomes greater as the modulation frequency increases. On the other hand, the transfer function of the baroreflex peripheral arc from SNA to AP shows "low-pass" characteristics, which means that the dynamic gain of the AP response to SNA variation becomes smaller as the modulation frequency increases. In short, the neural arc provides an accelerating mechanism of the dynamic AP response in the arterial baroreflex system [1].

Although a number of studies have indicated that the baroreflex function is depressed in heart failure [3–6], dynamic characteristics of the arterial baroreflex in heart failure have not been fully described. The aim of the present study was to identify the open-loop dynamic characteristics of the carotid sinus baroreflex in a rat model of chronic heart failure (CHF) after myocardial infarction. To obtain a total picture of the AP regulation in CHF, we also estimated the open-loop static characteristics of the carotid sinus baroreflex.

Materials and methods

Animals were cared for in strict accordance with the Guiding Principles for the Care and Use of Animals in the Field of Physiological Sciences, which has been approved by the Physiological Society of Japan. All experimental protocols were reviewed and approved by the Animal Subjects Committee at the National Cerebral and Cardiovascular Center.

Myocardial infarction

Coronary artery ligation was performed under sterile conditions in 8-week-old male Sprague-Dawley rats according to a previously established procedure [7]. After inducing anesthesia by halothane inhalation, the rat was intubated and mechanically ventilated. The left chest was opened at the fourth intercostal space and the left coronary artery was ligated with a 5-0 polypropylene suture (PROLENE, Ethicon, GA, USA). An electrocardiogram was monitored for 1 h after the coronary ligation, and the heart was defibrillated as necessary by manual prodding. Thereafter air was evacuated from the thoracic cavity and the incision was closed. The rats were allowed to recover from anesthesia, and were fed ad libitum with a standard laboratory chow and given free access to water. Although we initially planned to wait until the rats showed an objective sign of advanced heart failure such as facial edema or labored breathing, the rats with such severe heart failure were too weak to survive the acute baroreflex study described in the following section. Accordingly, the rats that survived for 100–200 days (156 ± 18 days) after myocardial infarction were used without solid criteria for starting the acute baroreflex study. Instead, the rats were regarded as experiencing CHF when the central venous pressure was higher than 2.5 mmHg or the biventricular weight was greater than 2.5 g/kg body weight at the time of the acute baroreflex study.

Acute baroreflex study

Experiments were performed in normal control ($n = 12$) and CHF ($n = 7$) rats. Sham operation was not performed in the control rats. Among the control rats, eight rats were matched with the CHF rats based on body weight, but they were younger in age due to the retardation of growth in the CHF rats. The remaining four rats were age-matched with the CHF rats, but they were heavier in body weight. Because none of the parameters of the baroreflex dynamic and static characteristics differed statistically between the two subgroups of the control rats, we report pooled data obtained from the 12 control rats.

Each rat was anesthetized with an intraperitoneal injection (2 ml/kg) of a mixture of urethane (250 mg/ml) and α-chloralose (40 mg/ml), and mechanically ventilated with oxygen-enriched room air. A venous catheter was inserted into the right femoral vein, and 20-fold diluted anesthetic mixture was administered continuously (2–3 ml kg^{-1} h^{-1}). An arterial catheter was inserted into the right femoral artery to measure AP. Heart rate (HR) was obtained from AP through a cardiotachometer. Another venous catheter was inserted into the left femoral vein and advanced into the inferior vena cava to measure central venous pressure and to supply Ringer solution (6 ml kg^{-1} h^{-1}).

A postganglionic branch from the splanchnic sympathetic nerve was exposed through a left flank incision, and a pair of stainless steel wire electrodes (Bioflex wire AS633, Cooner Wire, CA, USA) was attached to record SNA. The nerve and electrodes were covered with silicone glue (Kwik-Sil, World Precision Instruments, FL, USA) for insulation and fixation. To quantify the nerve activity, the preamplified nerve signal was band-pass filtered at 150–1,000 Hz, and then full-wave rectified and low-pass filtered with a cut-off frequency of 30 Hz. Pancuronium bromide (0.4 mg kg^{-1} h^{-1}) was administered to prevent muscular activity from contaminating the SNA recording. At the end of the experiment, we confirmed the disappearance of SNA in response to an intravenous bolus injection of a ganglionic blocker, hexamethonium bromide (60 mg kg^{-1}), and recorded the noise level.

Bilateral vagal and aortic depressor nerves were sectioned at the neck to avoid reflexes from the cardiopulmonary region and aortic arch. The carotid sinus regions were isolated from the systemic circulation bilaterally according to previously reported procedures [8, 9]. Briefly, a 7-0 polypropylene suture with a fine needle (PROLENE, Ethicon, GA, USA) was passed through the tissue between the external and internal carotid arteries, and the external carotid artery was ligated close to the carotid bifurcation. The internal carotid artery was embolized using two to three steel balls (0.8 mm in diameter, Tsubaki Nakashima, Nara, Japan) injected from the common carotid artery. Under these conditions, the brain stem area was perfused by patent bilateral vertebral arteries. The isolated carotid sinuses were filled with warmed Ringer solution through catheters inserted into the common carotid arteries. Carotid sinus pressure (CSP) was controlled using a servo-controlled piston pump. Heparin sodium (100 U kg^{-1}) was given intravenously to prevent blood coagulation. Body temperature was maintained at approximately 38°C with a heating pad.

Protocols

After the above surgical procedures were completed, reflex responses in SNA, AP, and HR to CSP input were

monitored for more than 30 min. The rat was excluded from further study and analysis in the event that the reflex responses became smaller within this period. Possible causes for the deterioration in the reflex responses include surgical damage to the carotid sinus nerves and brain ischemia due to the bilateral carotid occlusion.

To estimate the dynamic input-output relationship of the carotid sinus baroreflex, CSP was perturbed for 20 min using a Gaussian white noise (GWN) signal with the mean of 120 mmHg and standard deviation of 20 mmHg. The selection of the mean pressure and amplitude of GWN does not significantly affect the estimation of the system dynamic characteristics except for a factor of proportionality (see Appendix 1 for details). The switching interval of GWN was set at 500 ms. The input power spectral density was relatively constant up to 1 Hz, which covered the upper frequency range of interest with respect to the sympathetic arterial baroreflex in rats [2].

To estimate the static input-output relationship of the carotid sinus baroreflex, CSP was decreased to 60 mmHg for 4–6 min, and then increased stepwise from 60 to 180 mmHg in increments of 20 mmHg every minute [10].

Data analysis

Data were sampled at 200 Hz using a 16-bit analog-to-digital converter and stored on a dedicated laboratory computer system. In each rat, the noise level of SNA recorded after the administration of hexamethonium bromide was treated as zero. Because the absolute voltage of SNA varied among animals depending on the recording conditions, SNA averaged during the last 10 s at CSP of 60 mmHg in the stepwise input protocol was defined as 100%. The same normalization factor was used for the analysis of the baroreflex dynamic characteristics.

Dynamic characteristics of the baroreflex neural arc, peripheral arc, total baroreflex, and HR control were estimated by an open-loop transfer function analysis as follows [11]. Data were analyzed from 90 s after the initiation of the GWN input. The input-output data pairs were resampled at 10 Hz and segmented into 50% overlapping bins of 1,024 points each. For each segment, a linear trend was removed, and a Hanning window was applied. Fast Fourier transform was performed to obtain the frequency spectra of the input and output signals. The ensemble averages of the input power spectral density [$S_{XX}(f)$], output power spectral density [$S_{YY}(f)$], and cross spectral density between the input and output signals [$S_{YX}(f)$] were calculated over 12 segments, where f denotes frequency. Finally, the transfer function [$H(f)$] from input to output was estimated as:

$$H(f) = \frac{S_{YX}(f)}{S_{XX}(f)} \tag{1}$$

The transfer function is a complex-valued function that can be expressed by the modulus and phase at each frequency. In the present study, we refer to the modulus of the transfer function as the dynamic gain. To quantify the linear dependence between the input and output signals, a magnitude squared coherence function [Coh(f)] was calculated as:

$$\mathrm{Coh}(f) = \frac{|S_{YX}(f)|^2}{S_{XX}(f)S_{YY}(f)} \tag{2}$$

The coherence function is a real-valued function ranging from zero to unity. When the output signal is perfectly explained by the linear dynamics with the input signal, the coherence value becomes unity. When the output signal is totally independent of the input signal, the coherence value becomes zero.

To facilitate understanding of the transfer function, the step response was also calculated as follows. The system impulse response was derived from the inverse Fourier transform of $H(f)$. The step response was then obtained from the time integral of the impulse response.

To quantify the open-loop static characteristics of the carotid sinus baroreflex, mean SNA, AP, and HR were obtained during the last 10 s at each CSP level of the stepwise input protocol. In each rat, data from two consecutive step cycles were averaged. The static characteristics of the baroreflex neural arc (the CSP-SNA relationship), the total baroreflex (the CSP-AP relationship), and the HR control (the CSP-HR relationship) were described by fitting four-parameter logistic functions to the input-output data as follows [10, 12]:

$$y = \frac{P_1}{1 + \exp[P_2(x - P_3)]} + P_4 \tag{3}$$

where x and y denote the input (CSP) and output (SNA, AP, or HR), respectively; P_1 is the response range of output; P_2 is the slope coefficient; P_3 is the midpoint pressure of input; and P_4 is the minimum value of output. For convenience, the maximum slope or the maximum gain of the logistic function is reported by a positive value as $P_1P_2/4$.

The static characteristics of the baroreflex peripheral arc (the SNA-AP relationship) were quantified by a linear regression analysis as follows [10, 13]:

$$\mathrm{AP} = a \times \mathrm{SNA} + b \tag{4}$$

where a and b represent the slope and intercept, respectively, of the regression line.

Statistical analysis

All data are presented in mean and SE values. Unpaired t tests were used to compare the parameters of the baroreflex dynamic and static characteristics between the control and CHF groups [13]. To compare the transfer functions between the two groups, we arbitrarily selected the dynamic gain values at 0.01, 0.1, and 1 Hz ($G_{0.01}$, $G_{0.1}$, and G_1). For the step response relating to the neural arc transfer function, the negative peak response (S_{peak}), the time to the negative peak (T_{peak}), the value of the step response at 10 s (S_{10}), the steady-state response at 50 s (S_{50}), and the ratio of the peak response to the steady-state response (S_{peak}/S_{50}) were calculated. For the step response relating to the peripheral arc, total baroreflex, or HR control, an initial slope of the response was calculated (see Appendix 2) in addition to S_{50}. Differences were considered significant when $P < 0.05$.

Simulation study

Once the open-loop dynamic and static characteristics of a system are both identified, closed-loop system responses can be simulated [14–16]. To compare closed-loop behavior of the carotid sinus baroreflex between control and CHF conditions, step inputs ranging from −10 to −60 mmHg were applied as exogenous disturbances, and resulting AP responses were simulated. Percent recovery was calculated as the magnitude of steady-state AP recovery relative to the size of step disturbance. The initial slope for the recovery response was also calculated (see Appendix 2).

Results

Postmortem examination confirmed that the left ventricular free wall was reduced to a membrane-like scar in the CHF group. Biventricular weights, both absolute and relative to body weight, were significantly greater in the CHF than in the control group (Table 1). The central venous pressure was significantly higher and the baseline AP and HR were significantly lower in the CHF group. Although the duration after myocardial infarction ranged from 100 to 200 days in the CHF group, there was no significant correlation between the duration and biventricular weight ($y = 0.0012x + 2.53$, $r^2 = 0.035$, $P = 0.72$, x duration in days, y biventricular weight in grams per kilogram) or between the duration and central venous pressure ($y = -0.013x + 7.5$, $r^2 = 0.07$, $P = 0.58$, x duration in days, y central venous pressure in millmeters of mercury).

Typical experimental recordings obtained from a control rat are shown in Fig. 1a. m-SNA indicates a 2-s moving averaged signal of SNA. In the dynamic input protocol, CSP was changed dynamically according to a GWN signal. m-SNA varied dynamically in response to the CSP perturbation. Although AP changed dynamically, the AP variation seemed more sluggish than the SNA variation. Changes in HR were less obvious from the time series data. In the static input protocol, a stepwise increase in CSP decreased m-SNA, AP, and HR. The noise level of SNA obtained after the intravenous administration of hexamethonium bromide was set at zero. Because of the normalization procedure, m-SNA during the last 10 s at CSP of 60 mmHg approximated 100%. Figure 1b represents CSP and SNA signals sampled at 200 Hz during the dynamic input protocol. High CSP inputs suppressed SNA to a noise level.

Typical experimental recordings obtained from a CHF rat are shown in Fig. 2a. In the dynamic input protocol, CSP was changed dynamically according to a GWN signal. Although m-SNA varied dynamically in response to the CSP perturbation, changes in AP and HR were not obvious from the time series data. In the static input protocol, a stepwise increase in CSP decreased m-SNA, AP, and HR. The magnitudes of the responses in m-SNA, AP, and HR seem smaller than those in the control rat. Figure 2b represents CSP and SNA signals sampled at 200 Hz during the dynamic input protocol. High CSP inputs suppressed SNA to a noise level.

Dynamic characteristics of the carotid sinus baroreflex

Figure 3 summarizes the open-loop dynamic characteristics of the carotid sinus baroreflex averaged for the control

Table 1 Age, body weight, biventricular weight, central venous pressure, mean arterial pressure, and heart rate of the normal control and chronic heart failure (CHF) rats

	Control ($n = 12$)	CHF ($n = 7$)	P value
Age at experiment (weeks)	24 ± 3	30 ± 3	0.237
Body weight (g)	565 ± 28	538 ± 19	0.474
Biventricular weight (g)	1.16 ± 0.04	1.45 ± 0.08**	0.002
Biventricular weight (g kg body weight^{-1})	2.05 ± 0.06	2.71 ± 0.13**	<0.001
Central venous pressure (mmHg)	2.0 ± 0.2	5.4 ± 0.9**	<0.001
Mean arterial pressure (mmHg)	134 ± 4	121 ± 4*	0.037
Heart rate (beats min^{-1})	414 ± 11	350 ± 12**	0.001

Data are presented as mean ± SE

** $P < 0.01$ and * $P < 0.05$ by unpaired t test

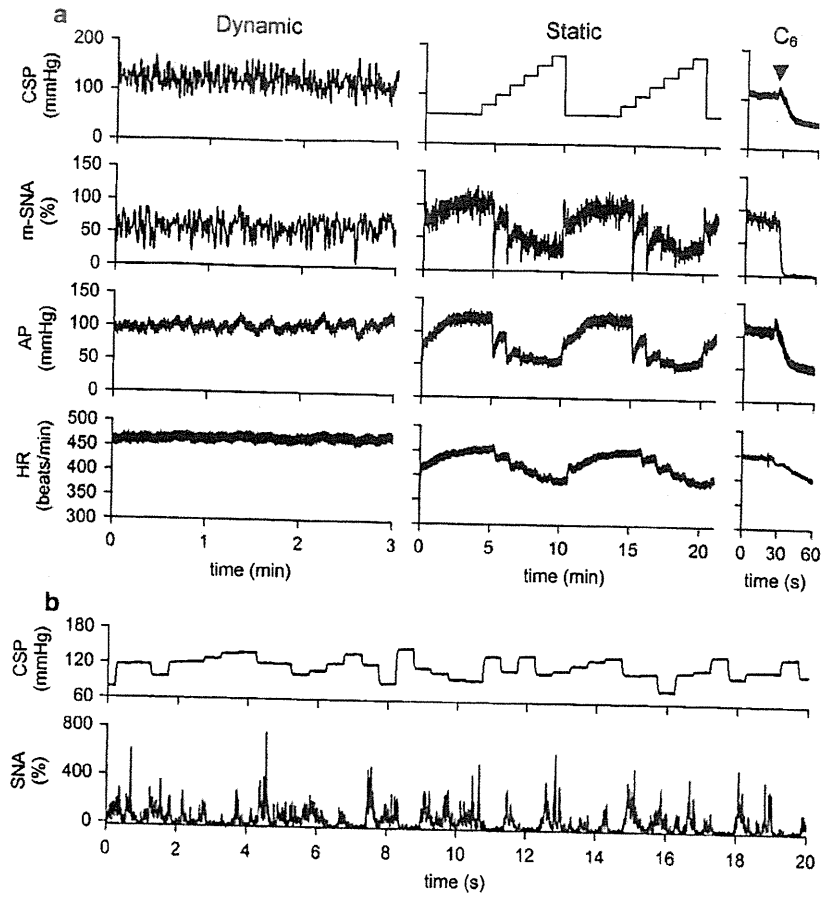

Fig. 1 **a** Typical recordings (10-Hz decimated data) of carotid sinus pressure (CSP), 2-s moving averaged sympathetic nerve activity (m-SNA), arterial pressure (AP), and heart rate (HR) obtained from a control rat. In the dynamic protocol, CSP was changed according to a Gaussian white noise signal. In the static protocol, CSP was increased from 60 to 180 mmHg. Hexamethonium bromide (C_6) was administered intravenously at the end of the experiment (*arrowheads*). The noise level of the nerve activity recorded after C_6 administration was assigned 0%, while the m-SNA value averaged for the last 10 s at CSP of 60 mmHg was assigned 100%. **b** CSP and SNA sampled at 200 Hz during the dynamic input protocol

and CHF rats. The neural arc transfer function from CSP to SNA showed derivative characteristics (Fig. 3a). $G_{0.01}$ tended to be lower in the CHF rats, whereas $G_{0.1}$ and G_1 did not differ significantly between the two groups (Table 2). The phase plot showed an out-of-phase relationship in the frequency range from 0.01 to 1 Hz in both groups. The coherence plot with values less than unity suggests that SNA contained an unknown noise signal unrelated to the baroreflex and/or a nonlinear system response to the CSP input. The bottom panel of Fig. 3a represents the step responses of SNA for a unit increase in CSP. Although S_{10} and S_{50} were significantly attenuated in the CHF rats, S_{peuk}, T_{peak}, and S_{peak}/S_{50} did not differ significantly between the two groups (Table 2).

The peripheral arc transfer function from SNA to AP showed low-pass characteristics (Fig. 3b). $G_{0.01}$ and $G_{0.1}$ were significantly smaller in the CHF rats, whereas G_1 did not differ significantly between the two groups (Table 2). The phase was close to zero radians at the lowest frequency and delayed with an increase in frequency in both groups. The coherence plot with values less than unity indicates that a part of AP variation was not explained by the linear dynamics with the SNA variation. In the step response of AP for a unit increase in SNA (Fig. 3b, bottom), S_{50} was significantly smaller and the initial slope (the dotted line) was significantly gentler in the CHF than in the control rats (Table 2).

The total baroreflex transfer function from CSP to AP showed low-pass characteristics (Fig. 3c). $G_{0.01}$ and $G_{0.1}$ were significantly smaller in the CHF than in the control rats (Table 2), but G_1 did not differ significantly. The phase was close to $-\pi$ radians at the lowest frequency in both groups, reflecting the negative feedback operation attained by the total baroreflex. The phase delayed with an increase in frequency. The coherence values seem lower than those in the peripheral arc transfer function. In the step response of AP for a unit increase in CSP (Fig. 3c, bottom), both S_{50} and the initial slope (the dotted line) were significantly attenuated in the CHF in comparison with the control rats (Table 2).

The transfer function from CSP to HR also displayed low-pass characteristics (Fig. 3d). $G_{0.01}$ and $G_{0.1}$ were significantly smaller in the CHF than in the control rats (Table 2). We did not compare G_1 because the coherence values close to zero and the irregular change in the phase shift above 0.8 Hz suggested poor reliability of the estimated transfer function. In the step response of HR for a unit increase in CSP (Fig. 3d, bottom), both S_{50} and the

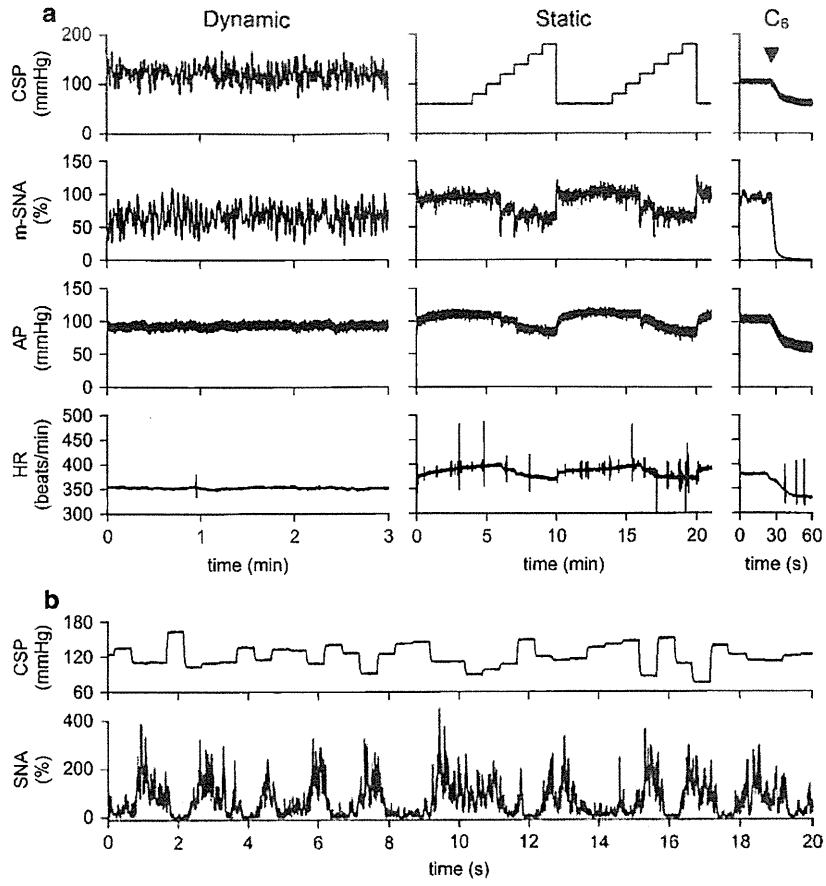

Fig. 2 a Typical recordings (10-Hz decimated data) of CSP, m-SNA, AP, and HR obtained from a chronic heart failure rat. In the dynamic protocol, CSP was changed according to a Gaussian white noise signal. In the static protocol, CSP was increased from 60 to 180 mmHg. The noise level of the nerve activity recorded after C_6 administration was assigned 0%, while the m-SNA value averaged for the last 10 s at CSP of 60 mmHg was assigned 100%. **b** CSP and SNA sampled at 200 Hz during the dynamic input protocol

initial slope (the dotted line) were significantly attenuated in the CHF in comparison with the control rats (Table 2).

Static characteristics of the carotid sinus baroreflex

Figure 4 summarizes the open-loop static characteristics of the carotid sinus baroreflex obtained from the control and CHF rats. The baroreflex neural arc showed a decreasing SNA response with an increase in CSP (Fig. 4a). The response range of SNA was significantly narrower in the CHF rats (Table 3). Consequently, the minimum SNA was significantly higher in the CHF rats. The midpoint pressure on the CSP axis was significantly lower in the CHF rats. Despite the significant attenuation in the response range of SNA, the maximum slope of the neural arc was not reduced in the CHF rats compared with the control rats.

The peripheral arc from SNA to AP approximated a straight line in both the control and CHF rats (Fig. 4b). The slope of the regression line was significantly less steep in the CHF rats, whereas the AP intercept did not differ significantly between the two groups (Table 3).

The total baroreflex function from CSP to AP approximated an inverse sigmoidal curve (Fig. 4c). The response range of AP was significantly narrower in the CHF rats (Table 3). The slope coefficient, the midpoint pressure on the CSP axis, and the minimum AP did not differ significantly between the two groups. The maximum gain was significantly smaller in the CHF rats compared with the control rats.

The static CSP-HR relationship also approximated an inverse sigmoidal curve (Fig. 4d). The response range of HR was significantly narrower, and the minimum HR was significantly lower in the CHF rats (Table 3). The midpoint pressure on the CSP axis was significantly lower in the CHF rats. The slope coefficient and the maximum slope did not differ significantly between the two groups.

The baroreflex equilibrium diagram is obtained by plotting the neural and peripheral arcs on a pressure-SNA plane (Fig. 4e). The ordinate is either CSP (for the neural arc) or AP (for the peripheral arc). The intersection between the neural and peripheral arcs gives the closed-loop operating point [17, 18]. The operating-point AP (the horizontal arrow) was significantly lower in the CHF rats, whereas the operating-point SNA (the vertical arrow) did not differ significantly between the two groups (Table 3). The total baroreflex gain at the operating point, calculated from the product of the tangential slope of the neural arc (ΔSNA/ΔCSP) and the slope of the peripheral arc (ΔAP/

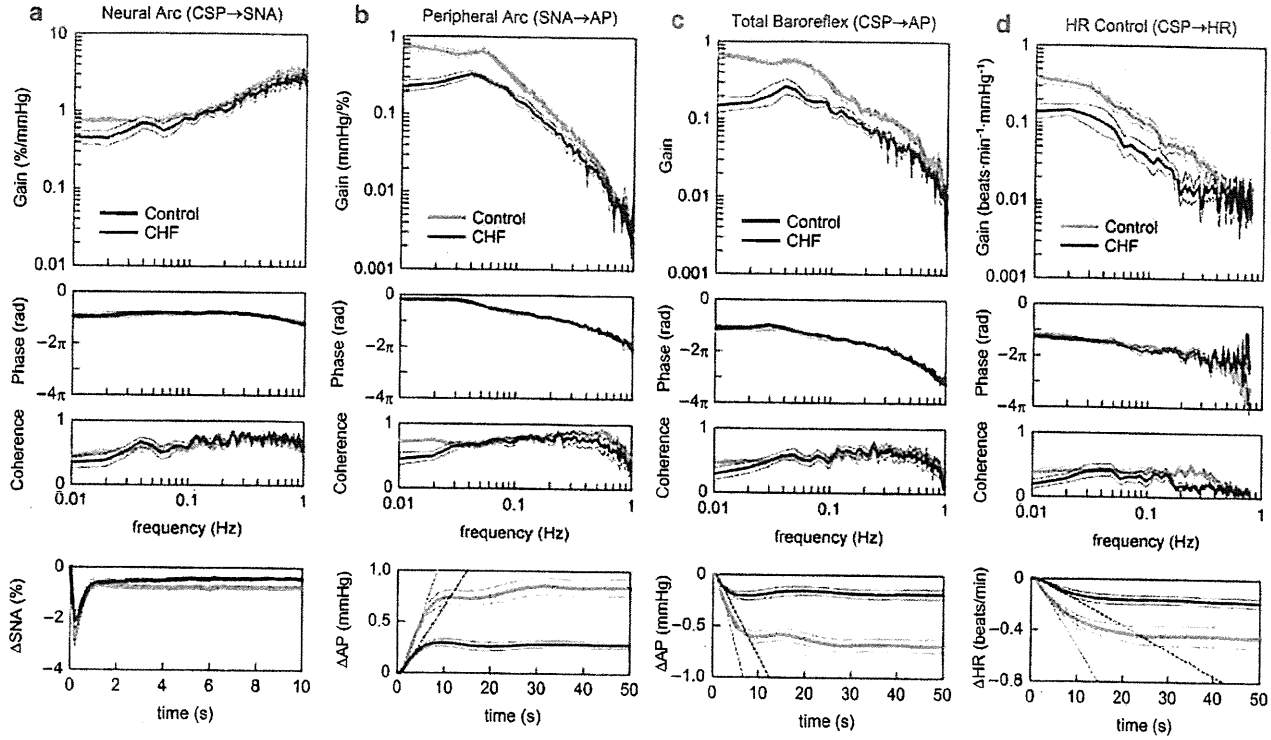

Fig. 3 Dynamic characteristics of the carotid sinus baroreflex averaged for the control rats ($n = 12$) and chronic heart failure (CHF) rats ($n = 7$). **a** Transfer function of the baroreflex neural arc from CSP to SNA. Gain, phase, and coherence plots are shown. The *bottom panel* represents the step response of SNA calculated from the transfer function. There is no significant difference in the negative peak response or the time to peak between control and CHF rats. **b** Transfer function of the baroreflex peripheral arc from SNA to AP. The *bottom panel* represents the step response of AP induced by a unit increase in SNA. Both initial slope (*dotted lines*) and steady-state response are attenuated in CHF. **c** Transfer function of the total baroreflex from CSP to AP. The *bottom panel* represents the step response of AP induced by a unit increase in CSP. Both initial slope (*dotted lines*) and steady-state response are attenuated in CHF. **d** Transfer function from CSP to HR. The *bottom panel* represents the HR step response calculated from the transfer function. Both initial slope (*dotted lines*) and steady-state response are attenuated in CHF. In each plot, *bold* and *thin lines* indicate mean and mean ± SE, respectively

ΔSNA), did not differ significantly between the two groups (Table 3): ΔCSP, ΔSNA, and ΔAP indicate small changes in CSP, SNA, and AP, respectively, at the intersection point. Figure 4f depicts a putative baroreflex equilibrium diagram where the SNA axis is scaled so that the maximum value of SNA in the CHF group becomes two times higher than that in the control group (see Discussion).

Simulation study

A block diagram of the simulation study is shown in Fig. 5a [14–16]. We used impulse responses derived from the group-averaged neural and peripheral arc transfer functions (H_N and H_P) to calculate dynamic responses of the carotid sinus baroreflex. The steady-state gains of H_N and H_P were normalized to unity in order that absolute values of the steady-state gains could be determined by their corresponding static characteristics. The static characteristics of the neural and peripheral arcs were modeled as a logistic function and a regression line, respectively, using group-averaged parameter values (Table 3). A sinusoidal wave with an amplitude of 15 mmHg (peak-to-peak pressure of 30 mmHg) and a frequency of 5 Hz (corresponding to 300 beats/min) was added to the output from the peripheral arc to mimic pulsatile pressure. The AP signal was fed back into the neural arc to achieve a closed-loop simulation. After the AP signal reached steady state, step disturbances ranging from −10 to −60 mmHg were imposed.

Typical examples of the transient AP response to a step disturbance of −40 mmHg under control and CHF conditions are shown in Fig. 5b. In each panel, the pulsatile pressure is shown in gray, and the mean AP signal is shown as a solid bold line. The horizontal dashed lines represent the mean AP values immediately before and after the onset of the step disturbance. The AP signal decreased abruptly by 40 mmHg at time zero and recovered gradually thereafter. The upward arrow indicates the magnitude of steady-state AP recovery. The recovery was greater in the control than in the CHF simulation.

Figure 5c depicts the percent recovery of AP relative to the size of the step disturbance. The steady-state AP

Table 2 Parameters of the dynamic characteristics of the carotid sinus baroreflex

	Control ($n = 12$)	CHF ($n = 7$)	P value
Neural arc			
$G_{0.01}$ (% mmHg^{-1})	0.80 ± 0.10	0.50 ± 0.08	0.051
$G_{0.1}$ (% mmHg^{-1})	0.99 ± 0.11	0.85 ± 0.14	0.432
G_1 (% mmHg^{-1})	3.49 ± 0.34	2.64 ± 0.30	0.093
S_{50} (%)	0.75 ± 0.09	0.39 ± 0.06*	0.012
S_{10} (%)	0.78 ± 0.09	0.42 ± 0.06*	0.010
S_{peak} (%)	2.88 ± 0.25	2.13 ± 0.30	0.076
T_{peak} (s)	0.29 ± 0.01	0.31 ± 0.01	0.327
S_{peak}/S_{50}	5.30 ± 1.60	6.06 ± 1.06	0.743
Peripheral arc			
$G_{0.01}$ (mmHg %$^{-1}$)	0.81 ± 0.09	0.24 ± 0.05**	<0.001
$G_{0.1}$ (mmHg %$^{-1}$)	0.29 ± 0.04	0.16 ± 0.02*	0.023
G_1 (mmHg %$^{-1}$)	0.0032 ± 0.0005	0.0050 ± 0.0015	0.211
S_{50} (mmHg)	0.84 ± 0.08	0.28 ± 0.03**	<0.001
Initial slope (mmHg s^{-1})	0.134 ± 0.014	0.071 ± 0.009**	0.007
Total baroreflex			
$G_{0.01}$ (mmHg mmHg^{-1})	0.70 ± 0.06	0.17 ± 0.03**	<0.001
$G_{0.1}$ (mmHg mmHg^{-1})	0.28 ± 0.03	0.13 ± 0.02**	0.001
G_1 (mmHg mmHg^{-1})	0.013 ± 0.002	0.010 ± 0.002	0.324
S_{50} (mmHg)	0.69 ± 0.07	0.18 ± 0.05**	<0.001
Initial slope (mmHg s^{-1})	0.166 ± 0.014	0.086 ± 0.009**	<0.001
Heart rate control			
$G_{0.01}$ (beats min^{-1} mmHg^{-1})	0.43 ± 0.06	0.16 ± 0.03**	0.005
$G_{0.1}$ (beats min^{-1} mmHg^{-1})	0.11 ± 0.02	0.04 ± 0.01*	0.026
S_{50} (beats min^{-1})	0.46 ± 0.08	0.18 ± 0.03*	0.021
Initial slope (beats min^{-1} s^{-1})	0.059 ± 0.009	0.020 ± 0.004**	0.006

Data are presented as mean ± SE

** $P < 0.01$ and *$P < 0.05$ by unpaired t test

recovery was approximately 50% in the control and approximately 32% in the CHF simulation for a step disturbance of −10 mmHg, indicating that the feedback AP regulation in the CHF simulation was approximately 64% as effective as that in the control simulation. On the other hand, the AP recovery was approximately 35% in the control and approximately 14% in the CHF simulation for a step disturbance of −60 mmHg, indicating that the efficiency of feedback AP regulation in the CHF simulation reduced to only 40% of that in the control simulation.

Figure 5d shows the initial slope of the AP recovery. The initial slope increased as the size of step disturbance increased in the control simulation. Although the initial slope of the AP recovery in the CHF simulation was comparable to that in the control simulation for a step disturbance of −10 mmHg, it did not increase significantly with an increase in the size of step disturbance.

Discussion

The major findings of the present study are (1) the dynamic characteristics of the baroreflex neural arc were preserved in CHF, whereas those of the baroreflex peripheral arc were significantly depressed (Fig. 3), and (2) the total baroreflex gain at the closed-loop operating point seemed preserved in CHF, whereas the range of baroreflex operation was significantly narrowed (Fig. 4). Because of these modulations in the baroreflex characteristics, the AP regulation was less robust against exogenous disturbances in CHF (Fig. 5), which may partly explain the incidence of acute decompensation in stable CHF patients caused by noncompliance with salt and water restriction [19].

Dynamic characteristics of the carotid sinus baroreflex in CHF rats

The derivative characteristics of the neural arc are preserved in the CHF rats (Fig. 3a), being consistent with a previous study in heart failure rabbits [20]. Moreover, the present results indicate that the dynamic AP response to SNA is significantly depressed in CHF (Fig. 3b), suggesting impaired end-organ responses to SNA. The total baroreflex function in terms of the AP regulation was more sluggish in the CHF rats (Fig. 3c, bottom) despite the preserved neural arc derivative characteristics.

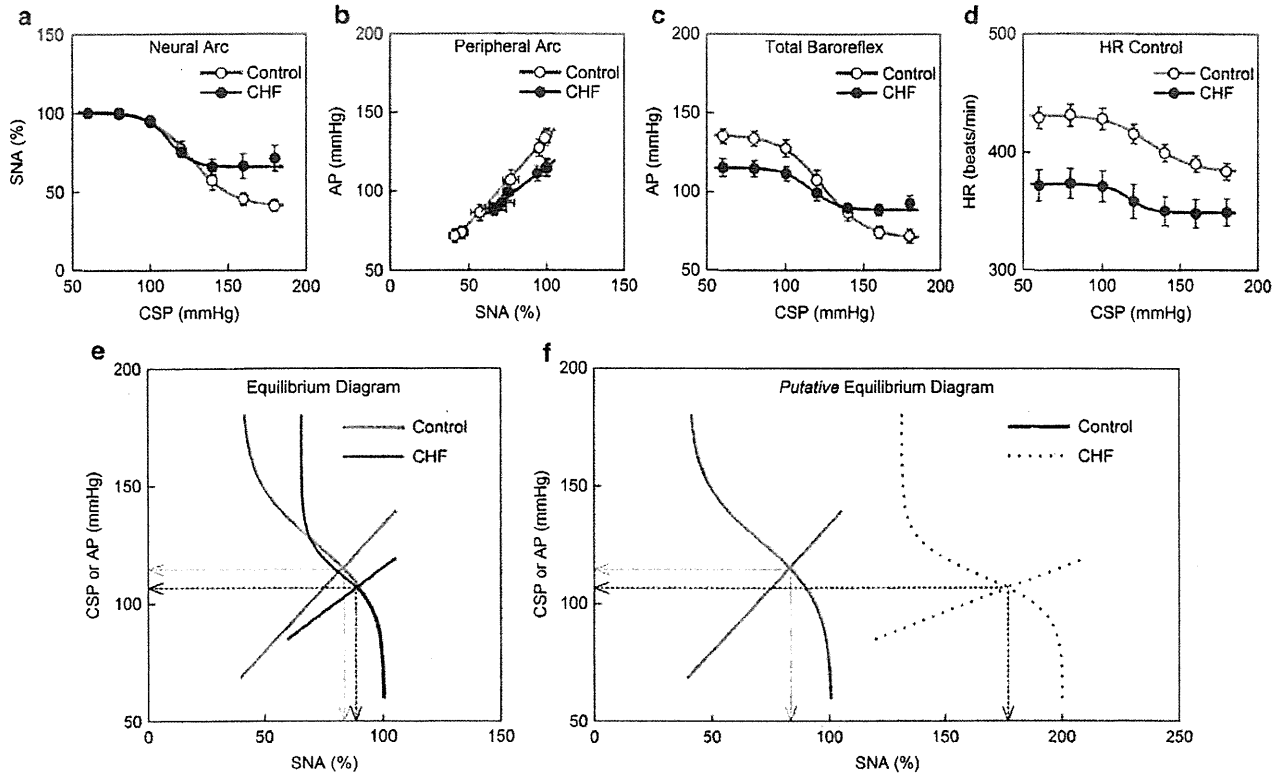

Fig. 4 Static characteristics of the carotid sinus baroreflex averaged for the control ($n = 12$) and chronic heart failure (CHF; $n = 7$) rats. **a** Static characteristics of the baroreflex neural arc. An increase in CSP decreases SNA. The response range in SNA is significantly attenuated in CHF. **b** Static characteristics of the baroreflex peripheral arc. An increase in SNA increases AP in a linear manner. The slope of the regression line is significantly gentler in CHF. **c** Static characteristics of the total baroreflex. CSP and AP show an inverse sigmoidal relationship. The response range of AP and the maximum gain are significantly smaller in CHF. **d** Static characteristics between CSP and HR. CSP and HR show an inverse sigmoidal relationship. The response range of HR and the minimum HR are significantly smaller in CHF. **e** Baroreflex equilibrium diagram constructed from the fitted logistic function for the neural arc and the regression line for the peripheral arc. **f** Putative baroreflex equilibrium diagram in which the SNA axis is scaled so that the maximum absolute SNA in CHF becomes two times higher than that in control. In panels **e** and **f**, the *dotted lines* with *arrowheads* indicate the operating-point AP and SNA in CHF. The *dash-dot lines* with *arrowheads* indicate the operating-point AP and SNA in control

In the transfer function from CSP to HR, dynamic gain values were significantly attenuated in the CHF rats (Fig. 3d). Because the dynamic gain of the neural arc transfer function did not reduce significantly ($G_{0.1}$), the attenuation of the dynamic gain of the HR control may be attributable to the reduced HR response to SNA such as that related to the downregulation of β-adrenergic receptors [21].

Static characteristics of the carotid sinus baroreflex in CHF rats

In both the control and CHF rats, the input-output relationship of the peripheral arc approximated a straight line (Fig. 4b), and the sigmoidal nonlinearity is primarily attributed to the neural arc (Fig. 4a). The impairment of the total baroreflex in the CHF rats, characterized by a significant attenuation of the response range of AP and a reduction of the maximum gain (Fig. 4c, Table 3), is in essence similar to that obtained previously in canine models of heart failure [3, 5, 6].

Wang et al. [4, 5] reported poor end-organ responses and normal central control of renal SNA in the heart failure dogs. The attenuated slope of the peripheral arc in the CHF rats (Fig. 4b) may be consistent with the poor end-organ responses. Although the response range of SNA in the neural arc was narrowed in the CHF rats (Fig. 4a), the maximum slope of the neural arc did not change significantly, which should contribute to the maintained total baroreflex gain within a small range around the operating point (Fig. 4e, Table 3).

The response range of HR was significantly reduced in the CHF rats (Fig. 4d) in agreement with the depressed dynamic HR response to CSP (Fig. 3d). Although 24-h averaged HR was higher in the CHF rats in a previous study [7], the minimum HR was significantly lower in the CHF than in the control rats. Anesthesia and vagotomy might have affected the results, and further studies are

Table 3 Parameters of the static characteristics of the carotid sinus baroreflex

	Control ($n = 12$)	CHF ($n = 7$)	P value
Neural arc			
P_1, response range (%)	62 ± 4	42 ± 6**	0.008
P_2, slope coefficient ($mmHg^{-1}$)	0.10 ± 0.01	0.16 ± 0.03*	0.048
P_3, midpoint pressure (mmHg)	128 ± 4	115 ± 4*	0.043
P_4, minimum SNA (%)	39 ± 4	60 ± 6**	0.008
Maximum slope (% $mmHg^{-1}$)	1.62 ± 0.27	1.54 ± 0.27	0.839
Peripheral arc			
a, slope (mmHg $\%^{-1}$)	1.10 ± 0.08	0.75 ± 0.10*	0.013
b, AP intercept (mmHg)	23.5 ± 7.7	40.7 ± 7.2	0.152
Total baroreflex			
P_1, response range (mmHg)	64 ± 4	31 ± 6**	<0.001
P_2, slope coefficient ($mmHg^{-1}$)	0.10 ± 0.01	0.13 ± 0.01	0.144
P_3, midpoint pressure (mmHg)	122 ± 3	117 ± 4	0.326
P_4, minimum AP (mmHg)	74 ± 4	85 ± 3	0.065
Maximum gain	1.62 ± 0.22	0.95 ± 0.17*	0.048
Heart rate control			
P_1, response range (beats min^{-1})	49 ± 5	30 ± 6*	0.033
P_2, slope coefficient (mmHg $^{-1}$)	0.10 ± 0.01	0.13 ± 0.01	0.099
P_3, midpoint pressure (mmHg)	131 ± 4	117 ± 4*	0.046
P_4, minimum HR (beats min^{-1})	383 ± 7	343 ± 13*	0.011
Maximum slope (beats min^{-1} $mmHg^{-1}$)	1.28 ± 0.23	0.93 ± 0.20	0.313
Equilibrium diagram			
Operating-point AP (mmHg)	116 ± 3	106 ± 3*	0.042
Operating-point SNA (%)	84 ± 3	90 ± 4	0.227
Operating-point total baroreflex gain	1.23 ± 0.28	0.96 ± 0.39	0.578

Data are presented as mean ± SE

** $P < 0.01$ and * $P < 0.05$ by unpaired t test

needed to reconcile some of the discrepancies between the present and previous results.

Equilibrium diagram and simulation study

A baroreflex equilibrium diagram provides information on the closed-loop operating point (Fig. 4e) [10, 17, 18, 22–26]. Because absolute SNA is considered to be higher in CHF [7], if we can use the absolute value for SNA, the SNA axis of the equilibrium diagram should be scaled in a manner that renders the peripheral arc much shallower in the CHF than in the control rats (Fig. 4f). The operating-point AP was decreased only by 10 mmHg in the CHF rats and the total baroreflex gain at the operating point did not differ between the control and CHF rats. The baroreflex function may therefore seem preserved in the CHF rats when it is assessed only within a small range around the closed-loop operating point.

We used splanchnic SNA to construct a baroreflex equilibrium diagram. The analysis based on SNA of only one limb of the sympathetic nervous system can be an oversimplification in light of the well-known regional differences in SNAs [27–29]. One rationale for using splanchnic SNA is that the splanchnic region has been regarded as a major site for the blood flow redistribution [17, 30]. Furthermore, we have continued to observe insignificant differences in the steady-state responses to CSP between left and right cardiac SNAs [31], between cardiac and renal SNAs [32], and among cardiac, renal, and muscle SNAs [33] in anesthetized rabbits. It seems that the carotid sinus baroreflex brings about common activity in addition to regional activity among sympathetic nerves innervating several districts (see Appendix 3). Whether the similarity among SNAs to different districts will hold in other experimental conditions awaits future investigations.

The simulation study is useful and necessary for the integrated understanding of the estimated dynamic and static characteristics of the carotid sinus baroreflex (Fig. 5a). The feedback AP regulation becomes much weaker in CHF as the size of step disturbance increases (Fig. 5c, d), suggesting that a reserve for AP buffering is lost in CHF. Because not only the baroreceptor input but also loading conditions to the heart are changed during orthostatic tilt, the results of the present simulation can not be directly extrapolated to the actual tilting conditions. However, it may be of notice that patients with severe congestive heart failure show a significant drop in systolic AP upon orthostatic tilt regardless of relatively maintained